



A General Materials Data Science Framework for Quantitative 2D Analysis of Particle Growth from Image Sequences

Sameera Nalin Venkat^{1,2} · Thomas G. Ciardi^{1,3} · Mingjian Lu^{1,3} · Preston C. DeLeo^{1,3} · Jube Augustino¹ · Adam Goodman¹ · Jayvic Cristian Jimenez^{1,2} · Anirban Mondal^{1,4} · Frank Ernst^{1,2} · Christine A. Orme⁵ · Yinghui Wu^{1,3} · Roger H. French^{1,2,3} · Laura S. Bruckman^{1,2}

Received: 30 October 2023 / Accepted: 3 January 2024 / Published online: 20 February 2024
© The Author(s) 2024

Abstract

Phase transformations are a challenging problem in materials science, which lead to changes in properties and may impact performance of material systems in various applications. We introduce a general framework for the analysis of particle growth kinetics by utilizing concepts from machine learning and graph theory. As a model system, we use image sequences of atomic force microscopy showing the crystallization of an amorphous fluoroelastomer film. To identify crystalline particles in an amorphous matrix and track the temporal evolution of the particle dispersion, we have developed quantitative methods of 2D analysis. 700 image sequences were analyzed using a neural network architecture, achieving 0.97 pixel-wise classification accuracy as a measure of the correctly classified pixels. The growth kinetics of isolated and impinged particles were tracked throughout time using these image sequences. The relationship between image sequences and spatiotemporal graph representations was explored to identify the proximity of crystallites from each other. The framework enables the analysis of all image sequences without the requirement of sampling for specific particles or timesteps for various materials systems.

Keywords Image analysis · Particle growth kinetics · Materials data science

✉ Laura S. Bruckman
lsh41@case.edu

Sameera Nalin Venkat
sxn440@case.edu

Thomas G. Ciardi
tgc17@case.edu

Mingjian Lu
mxl1171@case.edu

Preston C. DeLeo
pcd42@case.edu

Jube Augustino
jja92@case.edu

Adam Goodman
aig28@case.edu

Jayvic Cristian Jimenez
jxj440@case.edu

Anirban Mondal
axm912@case.edu

Frank Ernst
fxe5@case.edu

Christine A. Orme
ormel@llnl.gov

Yinghui Wu
yxw1650@case.edu

Roger H. French
rxf131@case.edu

- ¹ Materials Data Science for Stockpile Stewardship: Center of Excellence, Case Western Reserve University (CWRU), Cleveland, OH 44106, USA
- ² Department of Materials Science and Engineering, CWRU, Cleveland, OH 44106, USA
- ³ Department of Computer and Data Sciences, CWRU, Cleveland, OH 44106, USA
- ⁴ Department of Mathematics, Applied Mathematics and Statistics, CWRU, Cleveland, OH 44106, USA
- ⁵ Physical and Life Sciences Directorate, Lawrence Livermore National Laboratory, Livermore, CA 94550, USA

Introduction

Significant advances in experimental and computational methods have led to a rise in the quantity and complexity of information-rich materials datasets. The datasets present major challenges in processing and extracting information that can advance our understanding of the underlying mechanisms of complex processes in material systems. Therefore, it is imperative to store large datasets and process them effectively. To handle the quantity and complexity of datasets, there has been a gradual shift in materials research from an empirical science to data-driven science [1–4]. The shift led to the emergence of an interdisciplinary field called materials data science, in which data science techniques are implemented to solve materials science problems [5, 6].

The primary objective of materials data science is to mine large materials datasets to extract high-value and useful insights about the material system under consideration. Materials datasets are diverse and multimodal in nature, ranging from tabular data to images. In particular, data from various microscopy techniques provide valuable source of real-space information that captures and quantifies the temporal evolution of phase transformations in materials [6, 7].

One of the widely explored topics in materials science is the phase transformations in systems spanning from metals to polymers [8–14]. Phase transformations, such as the nucleation and growth of particles, play a critical role in determining the properties of material systems. Understanding the growth kinetics of phase transformations is essential for developing new materials with desired properties.

The evolution of particle growth can be tracked using various techniques including microscopy [14–16], which can lead to the generation of large datasets. To efficiently analyze large batches of microscopy data capturing particle growth, deep learning (DL) methods can be employed to obtain materials parameters of interest, such as areas of particles and their temporal evolution. DL is a specialized subset of machine learning, wherein neural networks are used to learn effective representations of data [17]. The concepts of DL can be extended for image analysis tasks. The applications of DL have been demonstrated in different fields, such as medicine and astrophysics in which image data is ubiquitous [18–22].

In recent years, DL has been applied to microscopy image processing of material systems. Out of the different DL architectures for image processing, U-Nets have gained traction in the research community because they require a minimal number of training images for a strong baseline performance [23]. Neural networks can perform

image segmentation to identify and locate desired features within an image. The neural network takes an image as an input and produces a pixel-wise mask to highlight the pixel location corresponding to a desired feature. In prior materials science research, U-Nets have been used in detection of grain boundaries in microscopy images of polycrystalline materials [24] and metallographic image analysis [25]. In this work, we use a U-Net variant for distinguishing particles that grow from amorphous matrix. Since U-Nets treat all detected particles as a single class, we also implemented connected components, an algorithm that uses pixel neighbors of the same value to identify distinct particles [26].

Since the growth of particles is impacted by surrounding particles, physical impingement and concentration gradients that extend out from the edges of the particles may lead to growth anisotropy. To measure such cooperative effects of particle growth by including environmental influences due to nearest neighboring particles, spatiotemporal graph (st-graph) representations provide a promising opportunity [27, 28]. st-graphs have the ability to capture the spatial and temporal relationships between individual entities, such as particles, in an ensemble [27]. In a simplistic st-graph representation, each particle can be represented as a node or vertex, and the spatial proximity between particles is encoded using edges between nodes. In this work, we use the nearest-neighbor distances between particles to define the edges in an st-graph. By incorporating the nearest-neighbor distances, we can effectively define the connections and relationships among the particles within the graph representation. Our work on st-graphs serves as a precursor to developing st-scene graphs [29] for particle behavior, which enables modeling relationships between particles. This framework is a step toward quantitatively capturing complex cooperative phenomena that will enable the field to move beyond particle growth theories focused on particles in isolation [30].

In this article, we present our modular materials data science framework that primarily involves image analysis, particle growth analysis, and representation of image sequences as st-graphs. We implement this framework to study the crystallization of a fluoroelastomer (FK-800), a binder in batteries, insulation layers, water barriers, and anti-fouling coatings. In systems like FK-800, phase transformations indicate formation of particles (crystallites) in an amorphous matrix. In FK-800, the amorphous-to-crystalline phase transformation alters the mechanical properties and may affect its overall performance [31].

Using the framework, we detected twelve unique crystallites over 700 image sequences using a U-Net variant, achieving 0.97 level of confidence in pixel-wise classification accuracy. Pixel-wise classification accuracy will be referred to as accuracy throughout this article. We were able

to track the growth kinetics as isolated or impinged crystallites over time. We explored st-graph representations over different timesteps to understand the proximity of crystallites during the growth process. We assimilated our work to develop a visual query tool in which the user can query any timestep to see the relationship of an image sequence to the corresponding st-graph representation and growth kinetics. The visual query tool is published as a Python package on PyPI repository [32]. We are able to analyze all the image sequences and crystallites at one go, enabling detailed insights into the growth kinetics.

Methods

Experimental Methods

FK-800 is a co-polymer of chlorotrifluoroethylene (CTFE) and vinylidene fluoride (VDF), with a CTFE:VDF ratio of 3:1 [33]. Between the glass transition temperature (~ 28 °C) and the melt temperature (~ 110 °C), the fluoroelastomer rearranges and crystallizes. The fluoroelastomer sample was prepared by dissolving 0.5 wt % FK-800 powder into ethyl acetate under ambient conditions and stirring it using a magnetic stir bar for ~ 2 h. To generate a film, 5 μL of solution was dropped onto a plasma-cleaned 10×10 mm silicon wafer and then immediately spun at 2450 rpm for 3 s and 8000 rpm for 30 s. Samples were then annealed at 125 °C for 1 h and rapidly quenched into liquid nitrogen-cooled water to generate an amorphous film. This process resulted in an ~ 50 nm thick amorphous film on a silicon substrate.

Atomic force microscopy (AFM) image sequences were captured using an Oxford Instruments Asylum Research Cypher ES equipped with a hot-stage set to 50.0 ± 0.2 °C. We acquired image sequences in tapping mode using an AC160 cantilever at a scan rate of 1.96 line Hz, resulting in an image acquisition time of 261 s. Due to the slow growth of the crystallites (< 0.02 nm/s), there were no measurable changes during the image acquisition time. The lateral pixel resolution for the $2 \times 2 \mu\text{m}^2$ area was about 4 nm and the tip radius had a nominal value of about 7 nm, resulting in an image resolution of ~ 10 nm.

The image sequences generated by the equipment were saved as an IGOR Pro (Wavemetrics) Binary Wave or .ibw file by default. These .ibw files were preprocessed to extract the images as TIFF files and metadata in .csv files. The resulting TIFF files had a pixel resolution of 512×512 . A total of 1200 images sequences were extracted. The dataset was reduced to the first 700 images from the sequence, since full crystallization is achieved then and later images are redundant. We have used the AFM height images in this study, although complimentary amplitude

and phase images may also be used in our future work. Times refer to the start time of the image (± 0.5 s). Time differences between images were approximated as the difference between start times.

Forty-six AFM height images were manually labeled using the polygon tool in LabelMe to identify crystallites [34]. Annotations were extracted from LabelMe as JSON files that were converted into binary TIFF images to serve as the ground truth for model training. The annotated images were manually selected to ensure all stages of crystallite growth were represented within the dataset. The dataset was split into training, validation, test subsets, where the validation and test sets were each composed of four manually selected images. The validation and test images that were selected spanned all crystallite growth stages to provide robust evaluation statistics. The model was trained with and without data augmentation. For the data augmentation in the training process, images were randomly flipped, rotated, and had their brightness or contrast adjusted in each iteration.

Data Science Methods

We selected a U-Net architecture as our DL model to segment crystalline from amorphous regions. Our U-Net implementation is constructed with four encoder and four decoder blocks. Each encoder block is composed of a convolutional block followed by a max pooling layer. Each decoder block is composed of a transposed convolutional layer, concatenation layer, and convolutional block in that order. The convolutional blocks are composed of two convolutional layers with a kernel size of 3, where each convolutional layer is followed by a batch normalization layer and rectified linear unit (ReLU) activation. The network was implemented from scratch using TensorFlow.

The model was trained for 100 epochs with early stopping set to a patience of 10. Adam was used as the optimizer with a learning rate of 0.001 and binary cross-entropy was selected as our loss function. We measure model performance across four metrics: accuracy, precision, recall, and binary intersection over union (IoU), which are defined in terms of true positive (TP), true negative (TN), false positive (FP) and false negative (FN).

- Accuracy: The accuracy measures the proportion of correctly classified pixels overall.

$$\text{Accuracy} = \frac{\text{TP} + \text{TN}}{\text{TP} + \text{TN} + \text{FP} + \text{FN}} \quad (1)$$

- Precision: The precision evaluates the proportion of pixels classified as positive that are actually positive.

$$\text{Precision} = \frac{\text{TP}}{\text{TP} + \text{FP}} \quad (2)$$

- Recall: The recall calculates the proportion of actual positive pixels that are correctly classified.

$$\text{Recall} = \frac{\text{TP}}{\text{TP} + \text{FN}} \quad (3)$$

- Intersection over Union (IoU): The IoU, also known as the Jaccard index, calculates the proportion of overlap between the predicted segmentation mask and the ground truth mask.

$$\text{IoU} = \frac{\text{TP}}{\text{TP} + \text{FP} + \text{FN}} \quad (4)$$

The U-Net model predicts a probability map where each pixel is labeled from 0 to 1. This value is a confidence score of the particular pixel; 0 indicates no confidence and 1 indicates complete confidence that the pixel belongs to the crystallite class. We selected 0.5 as the threshold to binarize the resulting probability map to a binary mask, where each pixel is labeled as either crystallite or amorphous region.

The best performing model was saved based on validation metrics and used to generate predictions for all image sequences. After generating predictions for the full dataset, connected components was used to quantify the statistics of individual crystallites. The following statistics were recorded for each crystallite: area, centroid, bounding box, and edge coordinates. Since connected components relies on neighboring pixels, this means that if two pixels from different crystallites are next to one another, the algorithm will label them as a single crystallite.

To solve this issue, masks predicted by the U-Net model were processed to impute borders between crystallites. This post-processing procedure involved taking the final image sequence and manually annotating pixels that belonged to the amorphous region. This yielded a border mask that enforced division between crystallites that appear visually merged. Since a pixel which is part of the amorphous region in the final image sequence will also be part of the amorphous

region in all previous image sequences, the border mask can be applied to all U-Net predictions across all the image sequences. This high-fidelity procedure ensured that borders between crystallites always existed and connected components captured crystallite statistics appropriately.

We calculated nearest-neighbor distances using Euclidean distances for each pair of crystallites in a matrix format. Given two sets of edge coordinates E_1 and E_2 , we constructed a Euclidean distance matrix between them and used the minimum value as the nearest-neighbor distance between a pair of crystallites. We generated the nearest-neighbor distances for all crystallites in a sequence of images.

The interface of the visual query tool was designed using NetworkX, a Python package for the creation, operation, visualization, and analysis of complex networks [35]. For the st-graph representations shown in this article, we used the igraph Python library along with NetworkX.

Results

The dataset we analyzed in this study consists of AFM image sequences that track the temporal evolution of a fluoroelastomer film while heating.

Figure 1 shows the nucleation and growth of crystallites from an amorphous FK-800 film. Nucleation likely occurs on the defect sites and expands in time to form crystallites. The crystallites typically rise 10–15 nm above the amorphous film and appear as lighter colors in the height images. As the crystallites grow, they consume material near their growth front, leading to a depleted zone (darker colors) at their edges. In our analysis, we approximate the film as having two components (amorphous and crystalline), and include the depleted zone as part of the amorphous phase. In our future work, we will treat the depleted zone as a third component. We also approximate the particles as two-dimensional because the lateral dimensions (in microns) are much greater than the height (<25 nm).

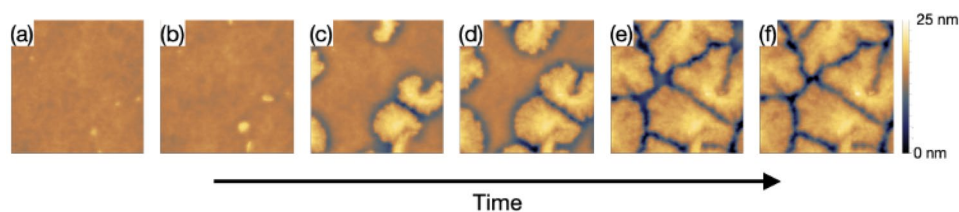
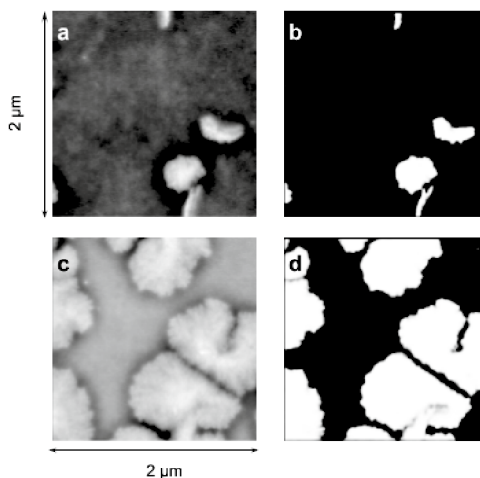


Fig. 1 Hot-stage atomic force microscopy (AFM) height image sequences illustrating the nucleation and growth in FK-800 fluoroelastomer. **a** At the beginning, the film is predominately amorphous. Crystallites grow after thermal aging at 50.0°C for **b** 1 h, **c** 8 h, **d**

12 h, **e** 1 day, and **f** 2 days. All images have a field of view of $2 \times 2 \mu\text{m}^2$ and a false-color z-scale of 25 nm (shown at the right). Times are precise to within 300 s and temperature is accurate to $\pm 0.2^\circ\text{C}$

Fig. 2 AFM height images (a, c) and corresponding U-Net predictions (b, d) at two time steps. a, b Timestep 67 corresponds to an image start time of 14050 s and c, d timestep 236 corresponds to an image start time of 49492 s. The table shows the evaluation parameters for U-Net predictions



Data Augmentation	Accuracy	Precision	Recall	Binary IoU
No	0.97	0.98	0.96	0.95
Yes	0.94	0.9	0.98	0.89

Figure 2 illustrates the AFM images and the corresponding U-Net predictions obtained by segmenting the image sequences. From the U-Net predictions, the crystallites are shown using white pixels and amorphous regions in black pixels. The AFM images represented in TIFF format, along with the corresponding U-Net prediction results, are displayed for two selected timesteps in the sequence. The AFM images are represented in grayscale with lighter colors representing the taller crystallites emerging from the amorphous region.

The accuracy of image segmentation is 0.94 with data augmentation and 0.97 without data augmentation. The data for the metrics that characterize the quality of the U-Net predictions have also been summarized.

Beyond categorizing crystalline and amorphous regions, we require identification of each individual crystallite to understand their temporal evolution. We have also categorized crystallites as isolated or impinged, and whether they are within or outside the field of view. Categorizing crystallites in such a manner enables crystallite tracking, quantification of crystallite kinetics, and allows us to flag crystallites that have different behavior. Over the entire range of time, we identified a total of twelve crystallites. Each crystallite was assigned a unique ID based on its nucleation time. The crystallites were labeled by numbers that reflect the sequence of their nucleation. Figure 3 shows the crystallite IDs for an image toward the end of the time period when the film is almost fully crystallized and the crystallites impinge each other. Crystallite 2 originally nucleated within the field of view and grew partially out of it over time. Other crystallites (such as crystallite 8) nucleated outside the field of view. Only crystallite 3 remained fully in frame throughout the crystallization process.



Fig. 3 Labels for crystallites formed during the crystallization process

To study phase transformations, the Avrami equation has been widely used [36]. Equation 5 shows the Avrami equation, where n is the Avrami exponent, k is the rate constant, y is the fraction of material transformed, and t is the time for the transformation to occur.

$$y = 1 - e^{-kt^n} \tag{5}$$

Fig. 4 shows the overall temporal progression of crystallization by plotting the fraction of the surface that is crystalline. The normalized areas throughout this study were obtained by dividing areas by the image dimensions. The Avrami equation has been used to fit the data corresponding to normalized total crystalline area versus time using $n = 2$ to represent 2D growth. The curve starts near zero, increases

Fig. 4 Normalized crystalline coverage versus time. The plot shows the fraction of the surface that is crystalline as determined by the U-Net model (gray dots). Avrami fitting is done for normalized area versus time. The blue line indicates the Avrami fit with using an Avrami exponent, $n = 2$

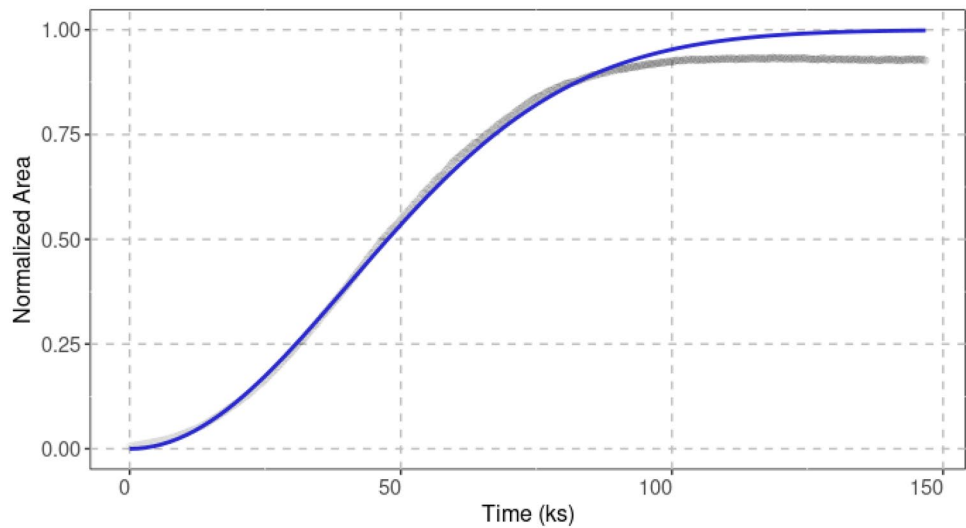
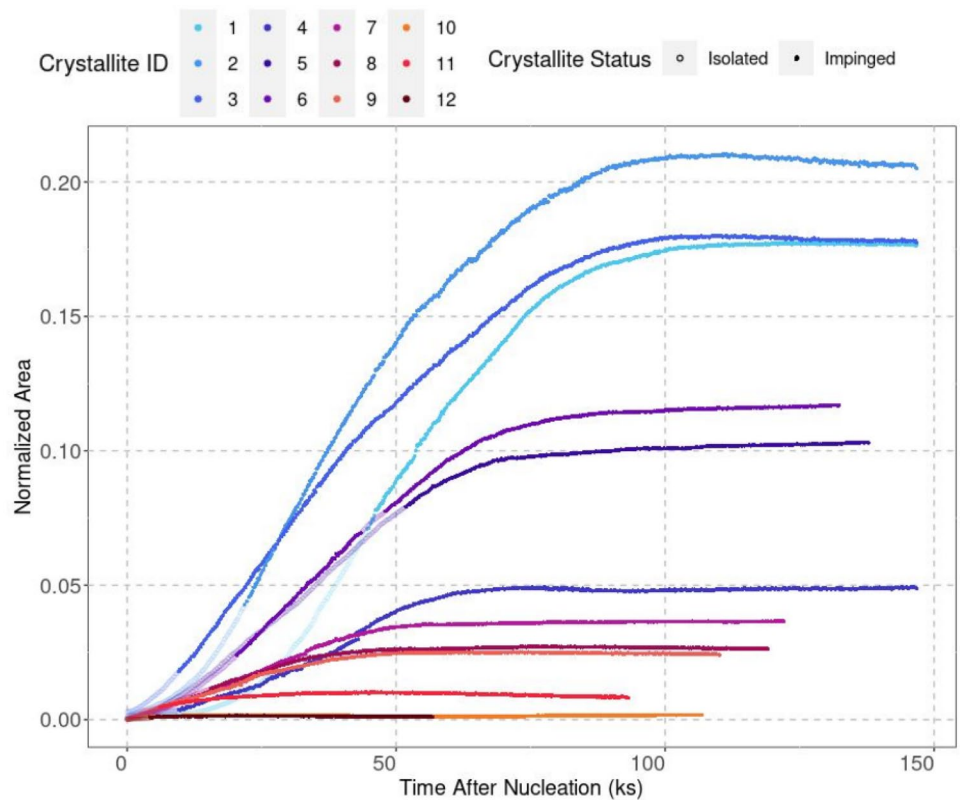


Fig. 5 Normalized areas of crystallites as a function of time after nucleation. Each curve represents a different crystallite ID. Isolated and impinged crystallites are denoted by open and solid points, respectively



rapidly initially, and then reaching a plateau. The estimated value of k obtained from the fitting is $3.1 \times 10^{-10} \text{ s}^{-2}$.

Figure 5 shows the temporal evolution of individual crystallite growth using normalized areas. Summing all of the crystallites leads to Fig. 4, such that at the final time of observation, the total normalized crystalline area approaches 1.00. Owing to different nucleation times, the total period of observation for each crystallites differs. Offsetting by the nucleation time allows us to compare curve shapes which

have substantial variation. The crystallite areas asymptotically approach a plateau, corresponding to the final crystallite size. We attribute the curve shape variation to several factors including anisotropic growth, impingement, and partial area measurements. We observed that only one out of twelve crystallites (crystallite 3) remain fully within the field of view over the entire period of observation. Crystallite 2 remains fully within the field of view only for the first 125 timesteps (26214 s).

To account for impingement, we investigated the kinetics of each crystal in the context of its nearest neighbors. Figure 5 displays the areas of crystallites as a function of time that are isolated or impinged by neighboring crystallites. The isolated crystallites are denoted by solid circles and impinged crystallites are denoted by open circles. The criterion for impingement is when two crystallites are separated by 10 px ($\sim 0.04 \mu\text{m}$) or less, which is approximately the width of the depleted zone. Once the crystallite gets impinged by a neighboring crystallite, we mark the crystallite as impinged and refer to it as first impingement. For each crystallite, the impingement due to neighboring crystallites occurs at different times. For this purpose, time after nucleation was considered to ensure that all the curves have a common starting time and are comparable. The crystallite areas increase slowly at first, then the increase rate goes through a maximum and then asymptotically approaches a plateau, corresponding to the final crystallite size.

Figure 6 shows the temporal evolution of effective radius for individual crystallites for isolated and impinged crystallites. The effective radius was obtained by approximating the 2D crystallite shape as a circle using $A = \pi r^2$, where A is

the crystallite area, and r is the effective radius. The overall curvature is similar to Fig. 5.

Using effective radii, we calculated effective radial growth rates for crystallites using the finite difference derivative of effective radii and times. Figure 7 shows the temporal variation of the effective radial growth rates (G_r) for isolated and impinged crystallites. Error bands were estimated based on error propagation for the finite difference derivative, where the primary error stems from the radial measurements and was assumed to be 1 pixel ($\sim 0.004 \mu\text{m}$). To minimize the time error, we used image sequences that were scanned in the same direction (i.e., both down) such that the differences in the image start time reflected the difference in time at any pixel position within the image. Hence, the effective radial growth rates were calculated for every 5 timesteps ($\sim 1305\text{s}$) to capture significant changes in radius over time.

In most cases, G_r of crystallites decreases monotonically in time, approaching zero as all edges of the crystallite become impinged or grow out of the field of view. However, for crystallites 1 and 2, G_r increases to a maximum value, decreases, and then approaches zero. We attribute this behavior to crystallites that nucleate with

Fig. 6 Temporal evolution of effective radii of crystallites. Each grid corresponds to a single crystallite. The crystallite status is distinguished based on when it is isolated (purple) and when it is first impinged (orange)

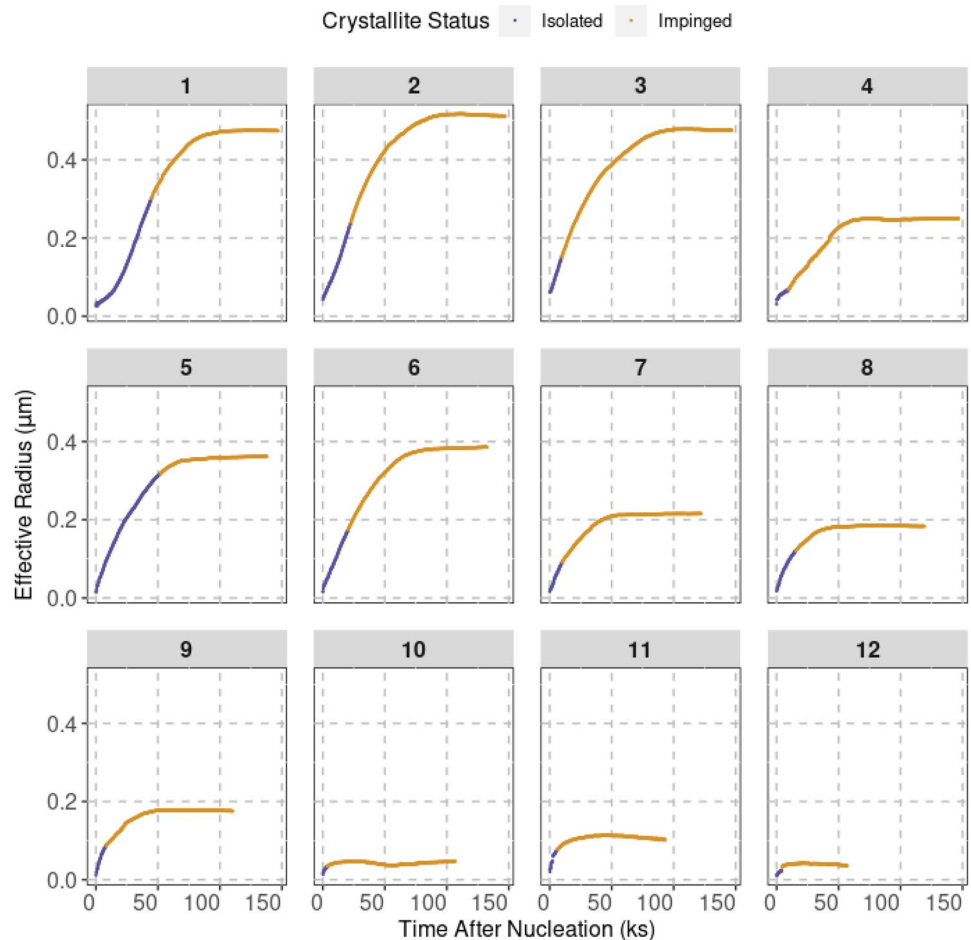
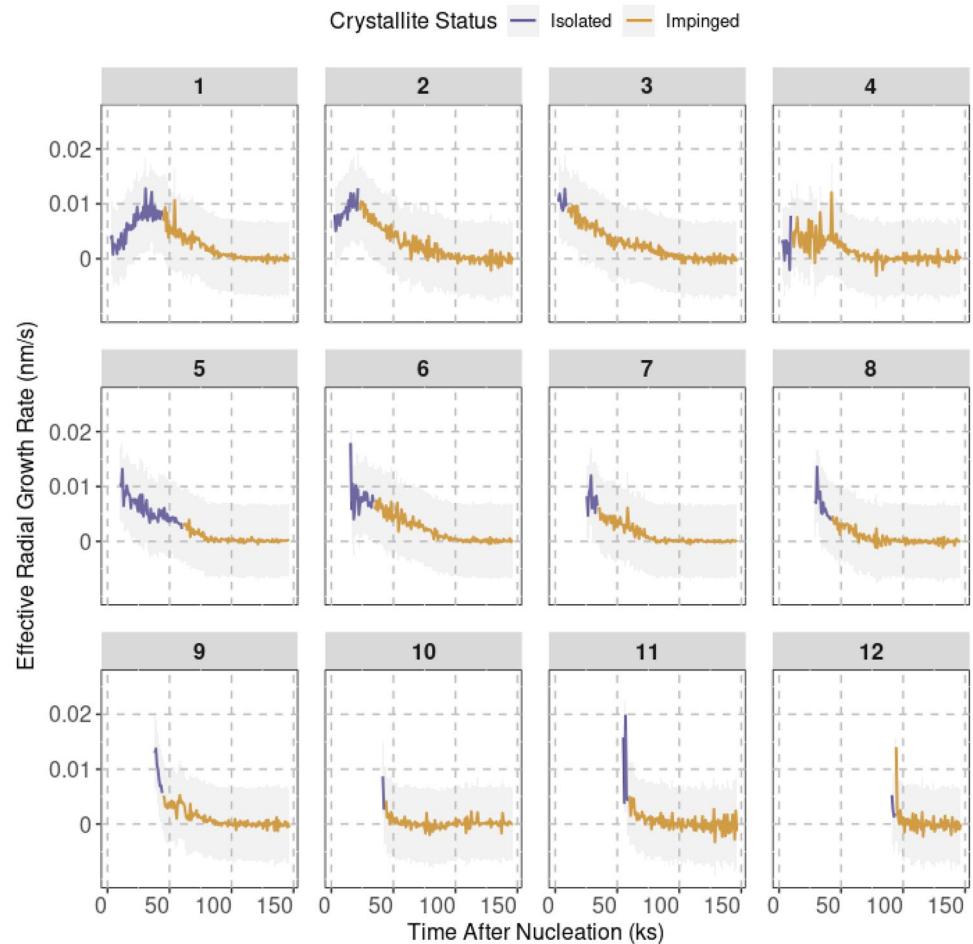


Fig. 7 Temporal evolution of effective radial growth rates over time with error bands (highlighted in gray). Each grid represents a crystallite. Isolated (purple) and impinged (orange) crystallites are captured in this plot



their fast growth direction perpendicular to the substrate plane rather than in the substrate plane. The propensity to nucleate vertically may be more likely in the initial stages of growth, as this behavior is observed for the crystallites that nucleated earlier. More statistics would be needed to verify this.

To quantify the proximity of crystallites from each other, we obtained st-graph representations for different timesteps. Figure 8 shows the relationship of AFM image sequences to the corresponding st-graph representations. The nodes in the graph show the crystallites and the presence of edges denote that the nearest neighbor distances between crystallites are less than 100 px ($\sim 0.4 \mu\text{m}$). These representations show the proximity of crystallites and formation of new crystallites over time.

We have assimilated the information from kinetics of crystallite growth and st-graphs into the visual query tool (MDS3-KGraph). The visual query tool lets the user go to any particular timestep of the crystallization process to observe the corresponding st-graph representation and kinetics until that timestep. We can obtain a summary of

crystallite characteristics, such as area and centroid, at any timestep. The visual query tool is available for usage on PyPI [32].

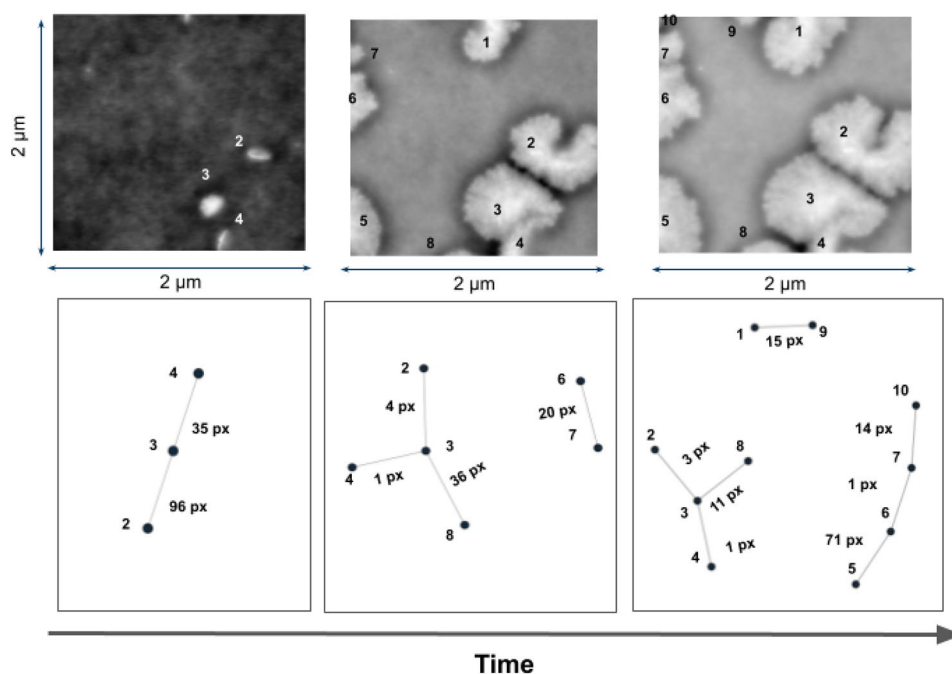
Discussion

We demonstrated different components of our modular materials science framework, which enables us to do image segmentation, particle growth analysis, and build st-graph representations. In this section, we explain some of the caveats for this type of analysis and discuss our results further.

Information about the Dataset

We conducted a 2D quantitative analysis of AFM height images. This is an approximation we used in our analysis, as AFM height images are three-dimensional in nature. The FK-800 fluoroelastomer film has crystallites that are less than 50 nm thick and have lateral dimensions in microns, so the crystallites can be approximated as 2D disks. The height

Fig. 8 AFM image sequences represented as spatiotemporal graph representations over time. The presence of edges mean that the nearest neighbor distances between crystallites are less than 100 px ($\sim 0.4 \mu\text{m}$). The pixel (px) values of the nearest neighbor distances are denoted in the figure



change in crystallites is negligibly small compared to the lateral change dimensions of growth. 2D analysis provides important information about areal coverage of crystallites, providing a useful starting point for future 3D analysis.

Although we can formally quantify individual crystallite areas over time and calculate effective radii and time-dependent effective radial growth rates, this dataset is not ideal for such detailed analyzes due to its narrow field of view. In an ideal situation, we would obtain the inherent effective radial growth rates from isolated crystallites that are not influenced by neighboring crystallites and remain fully within the field of view for accurate area measurements. Therefore, the conclusions we can draw regarding effective radial growth rates in this study are limited. However, we have demonstrated a viable framework for such a study using image sequences using AFM. This framework could be implemented for image sequences with a larger field of view or for data obtained using other imaging techniques, such as optical microscopy.

Even with these limitations, the framework enables us to calculate various growth characteristics like areas and effective radial growth rates for all crystallites across all the timesteps. In addition, we track isolated and impinged crystallites as well as crystallites growing in-frame or out of the image frame with time. This enables us to see the behavior of crystallites throughout time, without requiring us to sample certain crystallites or timesteps.

Analysis of Image Sequences

As crystallites grow and occupy space, they will invariably impinge upon each other at their growth fronts, slowing their growth rates. We define impingement when two crystallites are less than or equal to 10 px ($\sim 0.04 \mu\text{m}$). This was decided qualitatively by observing several crystallites and the depleted zones between pairs of crystallites. We have incorporated this information in our data, giving us a holistic picture of crystallite growth in the isolated and impinged cases.

We selected a U-Net variant as the DL image analysis method in this study. A key advantage of U-Nets are the use of a convolutional encoder-decoder architecture that allows efficient end-to-end learning by combining high resolution features from the input image with context from the downsampling path. This enables precise localization and segmentation of objects while also giving global context from the image. Given its demonstrated success in similar segmentation tasks, such as nuclei detection in medical imaging [37], U-Nets are an excellent choice to accurately identify and delineate the boundaries of our crystallite structures.

In another study, we have implemented You-Only-Once (YOLO) algorithm for crystallite detection and segmentation [38]. YOLO is fast at inference, being able to segment at over 30 frames per second (FPS). This speed comes from its single-shot design that divides the image into a grid and makes predictions for bounding boxes and class probabilities directly from full image context in one pass. While very fast, this grid design struggles to make

precise segmentation maps like U-Nets, especially for small, thin, or overlapping segmentation. Therefore, in a task where precision is more important than speed we choose the U-Net model.

The success of DL methods to identify crystallites enables several avenues for analysis that would be difficult, but not impossible if images were analyzed using manual methods. First, these analyzes can be used to quantify the crystalline and amorphous fractions of the the surface. We can obtain the surface-averaged time course of crystallization, which can be compared with crystallite growth models. Second, identification of individual crystallites allows comparison between them, opening up the possibility of quantifying statistical variations. Third, kinetics of individual crystallites can be investigated in the context of their neighbors, which is expected to be important when there are long-range interactions between crystallites. Although this particular dataset is not ideal for demonstrating all of these effects on fluoroelastomer crystallization kinetics, it is sufficiently complex to demonstrate the workflow, the issues, and the potential.

Our current image analysis approach contains some limitations. To validate across the dataset using the U-Net model, we selected four diverse images. This strategic selection was to maximize dissimilarity between images by considering different stages of growth, which allowed us to assess the robustness of the U-Net model. Expanding the validation set with images from different length scales, temperatures, and nucleation densities is important in our future work. This will provide a more comprehensive assessment of the model's generalizability and robustness. Currently, crystallite separation is enforced by imputing the final amorphous region across all the predictions. However, this requires a manual annotation of the final image and post-processing predicted masks, which is inefficient. Future directions might include leveraging instance segmentation rather than semantic segmentation, a weighted loss term to penalize erroneous borders, or alternative model architectures that can incorporate temporal information to distinguish boundaries.

Growth Behavior of the Entire System and Individual Crystallites

In Avrami fitting, we used an n value of 2 to approximate the crystallites as 2D disks. The same approximation was used in another similar study from our research group where YOLO was utilized [38].

In this study, we approximated the growth of these crystallites to be isotropic to simplify the calculation of the effective radius. Each individual crystallite is seen to have different rates of growth in different directions at different times, leading to growth anisotropy. The temperature and

concentration gradients associated with this phenomenon will be explored in a future study.

Crystallite geometries play an important role in our understanding of the fast growth directions. Crystallites that initiate out-of-plane transition into in-plane over time. We have not considered these aspects in our current work but we hope to explore these concepts in greater detail in our future work. In addition, we will explore different crystallite morphologies in our future work.

Conclusion

We have developed a general materials data science framework for the 2D analysis of particle growth. The novelty of our approach consists of employing deep learning and visualizing growth kinetics for image sequences without sampling for certain crystallites or timesteps. We have shown that this approach can be used for quantitative analysis of the temporal evolution of particle dispersions, especially the analysis of particle growth, and that the information can be effectively summarized in a visual query tool. The relationship between image sequences and spatiotemporal graphs could help us in understanding growth kinetics in the presence of neighboring crystallites and potential long-range interactions.

We implemented this general framework to investigate growth kinetics associated with the formation of crystallites in a fluoroelastomer film. It is critical to formulate an algorithm particle recognition (image segmentation) in order to avoid artifacts. We expect that the methods used in the study are suitable for studying growth kinetics of any general materials system.

Acknowledgements CO acknowledges useful discussions with En Ju Cho, Chami Swaminathan, Xiaojie Xu, and James Lewicki. Work performed by CO was under the auspices of the U.S. Department of Energy by Lawrence Livermore National Laboratory under Contract DE-AC52-07NA27344. This work made use of the High Performance Computing Resource in the Core Facility for Advanced Research Computing at Case Western Reserve University.

Author Contributions RF, LB, YW, FE, and AM led this research study and procured funding for accomplishing the work. SV, TC, ML, JJ, AM, FE, CO, YW, RF, and LB helped in conceptualization of ideas presented in this research work. CO was responsible for the curation of data. SV and JJ organized the collected data for analysis. SV, TC, ML, JA, AG, MM, and PD were primarily involved in the analysis of results covered in this study. All the authors helped in the different stages of manuscript development and editing and they approved the submitted version.

Funding This material is based upon research in the Materials Data Science for Stockpile Stewardship Center of Excellence (MDS³-COE), and supported by the Department of Energy's National Nuclear Security Administration under Award Number(s) DE-NA0004104.

Declarations

Conflict of interest The authors declare that there are no known financial interests or personal interests that could have influenced the work reported in this article.

Abridged Legal Disclaimer The views expressed herein do not necessarily represent the views of the U.S. Department of Energy or the United States Government.

Open Access This article is licensed under a Creative Commons Attribution 4.0 International License, which permits use, sharing, adaptation, distribution and reproduction in any medium or format, as long as you give appropriate credit to the original author(s) and the source, provide a link to the Creative Commons licence, and indicate if changes were made. The images or other third party material in this article are included in the article's Creative Commons licence, unless indicated otherwise in a credit line to the material. If material is not included in the article's Creative Commons licence and your intended use is not permitted by statutory regulation or exceeds the permitted use, you will need to obtain permission directly from the copyright holder. To view a copy of this licence, visit <http://creativecommons.org/licenses/by/4.0/>.

References

- Agrawal A, Choudhary A (2016) Perspective: materials informatics and big data: realization of the “fourth paradigm” of science in materials science. *APL Mater* 4(5):053208. <https://doi.org/10.1063/1.4946894>
- Wei J, Chu X, Sun X-Y, Xu K, Deng H-X, Chen J, Wei Z, Lei M (2019) Machine learning in materials science. *InfoMat* 1(3):338–358. <https://doi.org/10.1002/inf2.12028>
- Schleder GR, Padilha ACM, Acosta CM, Costa M, Fazzio A (2019) From DFT to machine learning: recent approaches to materials science—a review. *J Phys Mater* 2(3):032001. <https://doi.org/10.1088/2515-7639/ab084b>
- Himanen L, Geurts A, Foster AS, Rinke P (2019) Data-driven materials science: status, challenges, and perspectives. *Adv Sci* 6(21):1900808. <https://doi.org/10.1002/advs.201900808>
- Nihar A, Ciardi T, Chawla R, Chaudhary V, Wu Y, French RH (2023) Accelerating time to science using CRADLE: a framework for materials data science. In: Paper presented at the 30th IEEE international conference on high performance computing, data, & analytics. IEEE, Goa, India. <https://doi.org/10.1109/HiPC58850.2023.00041>
- Kalidindi SR, De Graef M (2015) Materials data science: current status and future outlook. *Annu Rev Mater Res* 45(1):171–193. <https://doi.org/10.1146/annurev-matsci-070214-020844>
- Ge M, Su F, Zhao Z, Su D (2020) Deep learning analysis on microscopic imaging in materials science. *Mater Today Nano* 11:100087. <https://doi.org/10.1016/j.mtnano.2020.100087>
- Tripathi PK, Maurya SK, Bhowmick S (2018) Role of disconnections in mobility of the austenite-ferrite interphase boundary in Fe. *Phys Rev Mater* 2(11):113403. <https://doi.org/10.1103/PhysRevMaterials.2.113403>
- Tripathi PK, Karewar S, Lo Y-C, Bhowmick S (2021) Role of interface morphology on the martensitic transformation in pure Fe. *Materialia* 16:101085. <https://doi.org/10.1016/j.mtla.2021.101085>
- Jeon S, Liu X, Azersky C, Ren J, Zhang S, Chen W, Hyers RW, Costa K, Kolbe M, Matson DM (2021) Particle size effects on dislocation density, microstructure, and phase transformation for high-entropy alloy powders. *Materialia* 18:101161. <https://doi.org/10.1016/j.mtla.2021.101161>
- Matsui M, Sakamoto K, Takahashi K, Hirano A, Takeda Y, Yamamoto O, Imanishi N (2014) Phase transformation of the garnet structured lithium ion conductor: $\text{Li}_7\text{La}_3\text{Zr}_2\text{O}_{12}$. *Solid State Ionics* 262:155–159. <https://doi.org/10.1016/j.ssi.2013.09.027>
- Li W, Qian X, Li J (2021) Phase transitions in 2D materials. *Nat Rev Mater* 6(9):829–846. <https://doi.org/10.1038/s41578-021-00304-0>
- Zhang H, Wang W, Xu T, Xu F, Sun L (2020) Phase transformation at controlled locations in nanowires by in situ electron irradiation. *Nano Res* 13(7):1912–1919. <https://doi.org/10.1007/s12274-020-2711-2>
- Hobbs JK, Farrance OE, Kailas L (2009) How atomic force microscopy has contributed to our understanding of polymer crystallization. *Polymer* 50(18):4281–4292. <https://doi.org/10.1016/j.polymer.2009.06.021>
- Kondekar N, Boebinger MG, Tian M, Kirmani MH, McDowell MT (2019) The effect of nickel on MoS₂ growth revealed with in situ transmission electron microscopy. *ACS Nano* 13(6):7117–7126. <https://doi.org/10.1021/acsnano.9b02528>
- Cecchi S, Lopez Garcia I, Mio AM, Zallo E, Abou El Kheir O, Calarco R, Bernasconi M, Nicotra G, Privitera SMS (2022) Crystallization and electrical properties of ge-rich GeSbTe alloys. *Nanomaterials* 12(4):631. <https://doi.org/10.3390/nano12040631>
- Erick M, Bannon D, Kudo T, Graf W, Covert M, Van Valen D (2019) Deep learning for cellular image analysis. *Nat Methods* 16:1233–1246. <https://doi.org/10.1038/s41592-019-0403-1>
- Alzubaidi L, Zhang J, Humaidi AJ, Al-Dujaili A, Duan Y, Al-Shamma O, Santamaria J, Fadhel MA, Al-Amidie M, Farhan L (2021) Review of deep learning: concepts, CNN architectures, challenges, applications, future directions. *J Big Data* 8(1):53. <https://doi.org/10.1186/s40537-021-00444-8>
- Shen D, Wu G, Suk H-I (2017) Deep learning in medical image analysis. *Annu Rev Biomed Eng* 19(1):221–248. <https://doi.org/10.1146/annurev-bioeng-071516-044442>
- Gómez-de-Mariscal E, Maška M, Kotrbová A, Pospíchalová V, Matula P, Muñoz-Barrutia A (2019) Deep-learning-based segmentation of small extracellular vesicles in transmission electron microscopy images. *Sci Rep* 9(1):13211. <https://doi.org/10.1038/s41598-019-49431-3>
- Hendriks L (2023) Deep learning based image analysis and anomaly detection in high energy physics and astrophysics. PhD thesis, Radboud University. Accepted: 2023-02-21. <https://repository.uibn.ru.nl/handle/2066/289688>
- Xing F, Xie Y, Su H, Liu F, Yang L (2018) Deep learning in microscopy image analysis: a survey. *IEEE Trans Neural Netw Learn Syst* 29(10):4550–4568. <https://doi.org/10.1109/TNNLS.2017.2766168>
- Ronneberger O, Fischer P, Brox T (2015) U-Net: convolutional networks for biomedical image segmentation. In: Navab N, Hornegger J, Wells WM, Frangi AF (eds) *Medical Image Computing and Computer-Assisted Intervention - MICCAI 2015*. Lecture Notes in Computer Science. Springer, Cham, p 234–241. https://doi.org/10.1007/978-3-319-24574-4_28
- Ma B, Liu C, Ban X, Wang H, Xue W, Huang H (2022) WPU-Net: boundary learning by using weighted propagation in convolution network. *J Comput Sci* 62:101709. <https://doi.org/10.1016/j.jocs.2022.101709>
- Biswas M, Pramanik R, Sen S, Sinitca A, Kaplun D, Sarkar R (2023) Microstructural segmentation using a union of attention guided U-Net models with different color transformed images. *Sci Rep* 13:1–14. <https://doi.org/10.1038/s41598-023-32318-9>
- He L, Ren X, Gao Q, Zhao X, Yao B, Chao Y (2017) The connected-component labeling problem: a review of state-of-the-art

- algorithms. *Pattern Recogn* 70:25–43. <https://doi.org/10.1016/j.patcog.2017.04.018>
27. Karimi AM, Wu Y, Koyuturk M, French RH (2021) Spatiotemporal graph neural network for performance prediction of photovoltaic power systems. In: *Proceedings of the AAAI conference on artificial intelligence*, vol 35. Association for the Advancement of Artificial Intelligence, Virtual, p 8. <https://doi.org/10.1609/aaai.v35i17.17799>
 28. Negro A (2021) *Graph-powered machine learning*. Manning Publications. <https://www.manning.com/books/graph-powered-machine-learning>
 29. Ji J, Krishna R, Fei-Fei L, Niebles JC (2019) Action genome: actions as composition of spatio-temporal scene graphs. *arXiv:1912.06992* [cs]
 30. Zhang MC, Guo B-H, Xu J (2017) A review on polymer crystallization theories. *Crystals* 7(1):4. <https://doi.org/10.3390/cryst7010004>
 31. Orme C, Bordia G, Lewicki J (2019) Developing experimental methods to measure phase change in fluoropolymer binders (Progress Summary). Technical Report LLNL-TR-772117, Lawrence Livermore National Lab. (LLNL), Livermore, CA (United States). <https://doi.org/10.2172/1544469>
 32. Lu M, Venkat SN, Ciardi T, Wu Y, French RH (2023) MDS3-KGraph. <https://pypi.org/project/mds3-kgraph/#description>
 33. Kristin K, Brown G, Anthony S (2020) Quantifying CTFE content in FK-800 using ATR-FTIR and time to peak crystallization. *Int J Polym Anal Charact* 25(8):621–633. <https://doi.org/10.1080/1023666X.2020.1827859>
 34. Russell BC, Torralba A, Murphy KP, Freeman WT (2008) LabelMe: a database and web-based tool for image annotation. *Int J Comput Vision* 77(1):157–173. <https://doi.org/10.1007/s11263-007-0090-8>
 35. Hagberg AA, Schult DA, Swart PJ (2008) Proceedings of the Python in science conference (SciPy): exploring network structure, dynamics, and function using NetworkX. In: *Proceedings of the 7th Python in science conference*, pp 11–15
 36. Avrami M (2004) Kinetics of phase change. I general theory. *J Chem Phys* 7(12):1103–1112. <https://doi.org/10.1063/1.1750380>
 37. Pandey R, Lalchhanhima R, Singh KR (2020) Nuclei cell semantic segmentation using deep learning Unet. In: *2020 advanced communication technologies and signal processing (ACTS)*, pp 1–6. <https://doi.org/10.1109/ACTS49415.2020.9350516>
 38. Mingjian L, Venkat SN, Augustino J, Meshnick D, Jimenez JC, Tripathi PK, Nihar A, Orme CA, French RH, Bruckman LS, Wu Y (2023) Image processing pipeline for fluoroelastomer crystallite detection in atomic force microscopy images. *Integr Mater Manuf Innov* 12:371–385. <https://doi.org/10.1007/s40192-023-00320-8>

Publisher's Note Springer Nature remains neutral with regard to jurisdictional claims in published maps and institutional affiliations.